

Fast and accurate prediction of numerical relativity waveforms from binary black hole coalescences using surrogate models

Jonathan Blackman,¹ Scott E. Field,² Chad R. Galley,¹ Béla Szilágyi,¹ Mark A. Scheel,¹ Manuel Tiglio,³ and Daniel A. Hemberger¹

¹TAPIR, Walter Burke Institute for Theoretical Physics, California Institute of Technology, Pasadena, CA 91125, USA

²Center for Radiophysics and Space Research, Cornell University, Ithaca, New York 14853, USA

³Center for Astrophysics and Space Sciences, Center for Computational Mathematics, San Diego Supercomputer Center, University of California San Diego, 9500 Gilman Drive, La Jolla, California 92093-0424, USA

(Dated: March 3, 2022)

Simulating a binary black hole (BBH) coalescence by solving Einstein’s equations is computationally expensive, requiring days to months of supercomputing time. Using reduced order modeling techniques, we construct an accurate surrogate model, which is evaluated in a millisecond to a second, for numerical relativity (NR) waveforms from non-spinning BBH coalescences with mass ratios in $[1, 10]$ and durations corresponding to about 15 orbits before merger. We assess the model’s uncertainty and show that our modeling strategy predicts NR waveforms *not* used for the surrogate’s training with errors nearly as small as the numerical error of the NR code. Our model includes all spherical-harmonic ${}_{-2}Y_{\ell m}$ waveform modes resolved by the NR code up to $\ell = 8$. We compare our surrogate model to Effective One Body waveforms from 50-300 M_{\odot} for advanced LIGO detectors and find that the surrogate is always more faithful (by at least an order of magnitude in most cases).

Since the breakthroughs of 2005 [1–3], tremendous progress in numerical relativity (NR) has led to hundreds of simulations of binary black hole (BBH) coalescences [4–10]. This progress has been driven partly by data analysis needs of advanced ground-based gravitational wave detectors like LIGO [11] and Virgo [12]. Recent upgrades to these detectors are expected to yield the first direct detections of gravitational waves (GWs) from compact binary coalescences [13].

Despite the remarkable progress of the NR community, a single high-quality simulation typically requires days to months of supercomputing time. This high computational cost makes it difficult to directly use NR waveforms for data analysis, except for injection studies [4, 9], since detecting GWs and inferring their source parameters may require thousands to millions of accurate gravitational waveforms. Nevertheless, a first template bank for nonspinning binaries in Advanced LIGO has been recently constructed from NR waveforms [14]. Furthermore, NR waveforms have been used successfully in calibrating inspiral-merger-ringdown (IMR) effective-one-body (EOB) [15–21] and phenomenological [22–25] models. These models have free parameters that can be set by matching to NR waveforms and are suitable for certain GW data analysis studies [26]. However, these models can have systematic errors since they assume *a priori* physical waveform structure and are calibrated and tested against a small set of NR simulations.

In this Letter, we present an *ab initio* methodology based on surrogate [27, 28] and reduced order modeling techniques [29–33] that is capable of accurately predicting the gravitational waveform outputs from NR *without* any phenomenological assumptions or approximations to general relativity. From a small set of specially selected non-spinning BBH simulations performed with

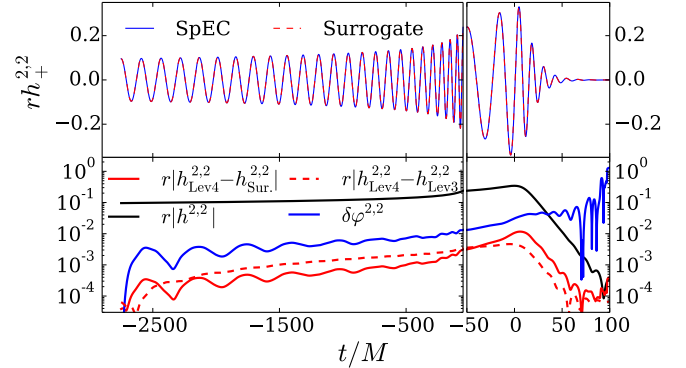


FIG. 1. **Top:** The $+$ polarization $(2,2)$ mode prediction for $q = 2$, the surrogate model’s worst prediction over q from a “leave-one-out” surrogate that was *not* trained with this waveform (see below). Our full surrogate, trained on the entire data set, is more accurate. **Bottom:** Phase $\delta\varphi^{2,2}$ and waveform differences between the surrogate and highest resolution (Lev4) SpEC waveforms. Also shown is the SpEC numerical truncation error found by comparing the two highest resolution (Lev4 and Lev3) waveforms.

the Spectral Einstein Code (SpEC) [34–36], we build a surrogate model that can be used in place of performing SpEC simulations. The techniques are general, however, and directly apply to other NR codes or even analytical waveform models. The surrogate model constructed here generates non-spinning BBH waveforms with mass ratios $q \in [1, 10]$, contains 25–31 gravitational wave cycles before peak amplitude, and includes many spherical-harmonic modes (see Table II and its caption). These choices are made based on available NR waveforms and are not limitations of the method. Our surrogate model has errors close to the estimated numerical error of the

input waveforms. An example comparing the surrogate output to an NR waveform can be seen in Fig. 1. This simulation took 9.3 days using 48 cores but only ~ 0.01 sec for the surrogate evaluation of the (2,2) mode.

Previous work [27, 37] built surrogates for EOB waveforms; building and assessing surrogate models of NR waveforms have unique challenges associated with input waveforms that are expensive to compute. We summarize next the construction of our model, focusing on steps not addressed in [27] but are required for NR surrogates.

Parametric sampling—Typically, a surrogate model is trained on a dense set of waveforms known as the *training set*. In the case of NR, we cannot afford to generate a large number of waveforms. Instead, we generate a dense set of non-spinning waveforms using an EOB model [18], as implemented in [38], which contains the $(\ell, m) = \{(2, 2), (2, 1), (3, 3), (4, 4), (5, 5)\}$ spin-weight -2 spherical-harmonic modes and captures robust features of NR waveforms. The EOB training set waveforms are computed for times in $[-2750, 100]M$ (M is the total mass), which is the interval over which we build our surrogates.

Next, on this training set we apply a greedy algorithm to expose the most relevant mass ratio values [39, 40]. The algorithm proceeds from a linear basis constructed from i waveforms already chosen. The L^2 norms of the differences between the training set waveforms and their projection onto this basis are computed. The waveform with the largest such error is added to the basis as its $i + 1$ element. SpEC simulations of non-spinning BBH mergers are then performed for these mass ratios. The resulting NR waveforms are used to build our surrogates without any further input from the EOB model.

We seeded the greedy algorithm with 5 publicly available SpEC simulations of non-spinning BBH mergers [10, 19] (see Table I), and the next 17 (ordered) mass ratio values are the algorithm’s output based on the EOB model. The final ~ 10 mass ratios are included to improve the surrogate if necessary, since we can assess the surrogate model’s accuracy only after it is built. Our method for building surrogates is hierarchical [27, 40]; additional NR waveforms can be included to improve the model’s accuracy.

Generating the NR waveforms—Table I summarizes the 22 SpEC simulations used in this paper. See, e.g., Ref. [35] for the numerical techniques used in SpEC. The numerical resolution is denoted by “Levi”, where i is an integer that controls the local truncation error in the metric and its derivatives allowed by adaptive mesh refinement (AMR) in SpEC; larger numbers correspond to smaller errors (the error threshold scales like e^{-i}) and more computationally-expensive simulations. The scaling of global quantities (e.g. waveform errors) with i is difficult to estimate *a priori*. Two to five levels of resolution are simulated for each mass ratio. To achieve quasi-circular orbits, initial data are subject to an itera-

#	ID	q	e_{-5}	T/M	Orbs	#	ID	q	e_{-5}	T/M	Orbs
1	180	1.00	5.1	9867	28.2	12	191	2.51	65	6645	22.5
2	181	6.00	5.8	7056	26.5	13	192	6.58	4.0	5149	21.1
3	182	4.00	12	3840	15.6	14	193	3.50	3.0	5242	19.6
4	183	3.00	4.8	4008	15.6	15	194	1.52	74	5774	19.6
5	184	2.00	15	4201	15.6	16	195	7.76	22	5226	21.9
6	185	9.99	31	5817	24.9	17	196	9.66	23	5330	23.1
7	186	8.27	16	5687	23.7	18	197	5.52	25	5061	20.3
8	187	5.04	3.0	4807	19.2	19	198	1.20	17	6315	20.7
9	188	7.19	15	5439	22.3	20	199	8.73	8.5	5302	22.6
10	189	9.17	13	6019	25.2	21	200	3.27	36	5507	20.2
11	190	4.50	2.5	5199	20.1	22	201	2.32	15	5719	20.0

TABLE I. Properties of the highest resolution SpEC simulations used for building BBH waveform surrogates. The quantity e_{-5} is the orbital eccentricity divided by 10^5 [43]. The duration T/M and number of orbits (Orbs) are also given. The SpEC simulations are available in the public waveform catalog [10] under the name “SXS:BBH:ID.”

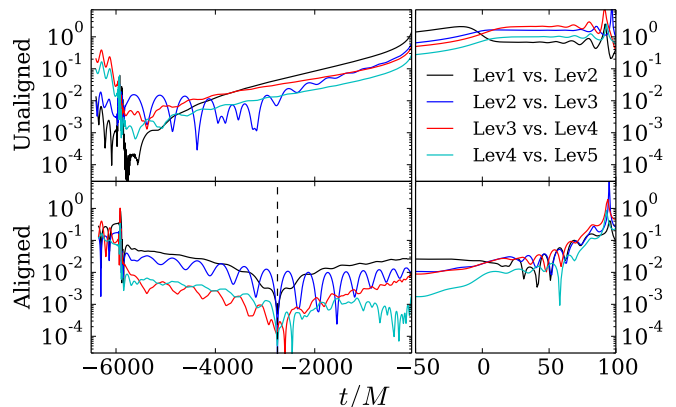


FIG. 2. The relative error, $|h_i^{22} - h_{i+1}^{22}|/|h_{i+1}^{22}|$, of successive resolutions SpEC Levi for the (2,2) mode of simulation 19 in Table I. **Top**: Waveform output as directly given by SpEC (“Unaligned”). **Bottom**: “Aligned,” which involves a multi-mode peak alignment scheme described by Eq. (2) followed by a rotation of the waveform around the z -axis to align the waveform phases at $t_i = -2750M$. Our surrogate is built from NR waveform data after alignment, and so this measurement of truncation error is the most relevant for surrogate model building.

tive eccentricity reduction procedure resulting in eccentricities $\lesssim 7 \times 10^{-4}$ [41–43].

SpEC numerically solves an initial boundary value problem defined on a finite computational domain. To obtain waveforms at future null infinity \mathcal{I}^+ , we use the Cauchy characteristic extraction (CCE) method [44–48]. Using the PittNull code [44–46], we compute the Newman-Penrose scalar Ψ_4 at \mathcal{I}^+ and finally obtain the gravitational wave strain h through two temporal integrations. We minimize the low-frequency, noise-induced

“drifts” [47] by using frequency cut-offs.¹

Figure 2 shows the convergence typically observed in our simulations when using AMR. Because AMR makes independent decisions for different Levi , a particular subdomain may sometimes have the same number of grid points for two different values of Levi at a given time, and the subdomain boundaries do not necessarily coincide for different Levi . Thus, plots like Figure 2 sometimes show anomalously small differences between particular pairs of numerical resolutions (for instance Lev2 vs. Lev3 near $t = -3500M$ in the top panel of Figure 2). See Sec. IIIB of [35]. Nevertheless, the waveform differences generally decrease quickly with increasing resolution. Let

$$\delta h^{\ell,m}(q) \equiv \frac{\|h_1^{\ell,m}(\cdot; q) - h_2^{\ell,m}(\cdot; q)\|^2}{\sum_{\ell,m} \|h_2^{\ell,m}(\cdot; q)\|^2} \quad (1)$$

be the disagreement between two waveform modes $h_1^{\ell,m}$ and $h_2^{\ell,m}$ where $\|h^{\ell,m}(\cdot; q)\|^2 = \int dt |h^{\ell,m}(t; q)|^2$. We estimate the numerical truncation error of each mode when h_1 and h_2 are waveforms computed at the two highest resolutions. The full waveform² error for a given mass ratio is $\delta h(q) = \sum_{\ell,m} \delta h^{\ell,m}(q)$. We report numerical truncation errors after an overall simulation-dependent time shift and rotation (which we shall refer to as *surrogate alignment*, described in the next section), which are physically unimportant coordinate changes. The resulting estimated numerical truncation errors of the dominant (2, 2) modes, using our surrogate alignment scheme, are shown in Fig. 3 (black circles).

Additional error sources are non-zero eccentricity in the (intended to be circular) NR initial data, and an imperfect procedure for integrating $\Psi_4^{\ell,m}$ to obtain $h^{\ell,m} \equiv A^{\ell,m} \exp(-i\varphi^{\ell,m})$. These both cause small oscillations in the waveform amplitudes $A^{\ell,m}(t)$ and phases $\varphi^{\ell,m}(t)$ [47, 50] that we model following [50]. We also compute the error in the strain integration scheme by comparing $\Psi_4^{\ell,m}$ to two time derivatives of $h^{\ell,m}$, as well as estimates for numerical errors in the CCE method [48]. For the (2, 2) mode, these additional errors are negligibly small compared to SpEC truncation errors (cf. Fig. 3).

Preparing NR waveforms for surrogate modeling– We apply a simulation-dependent time shift and physical rotation about the z -axis so that all the modes’ phases are aligned. This reveals the underlying parametric smoothness in q that will be useful for building a surrogate. Our

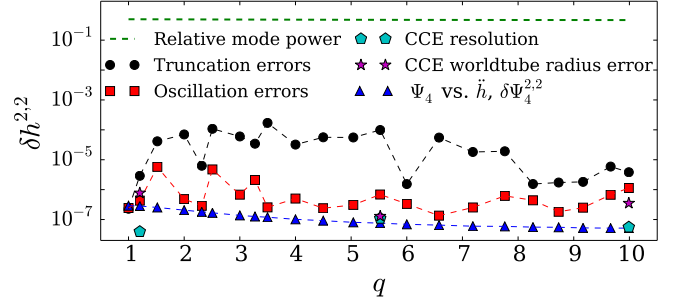


FIG. 3. Numerical truncation errors (black) dominate all other sources of error for the (2,2) mode, except for simulation 1 ($q = 1$), where the truncation errors are already very small. For some weaker modes, systematic amplitude oscillations primarily due to eccentricity may become more relevant.

time shifts set each waveform’s *total* amplitude

$$A(t; q)^2 \equiv \int_{S^2} d\Omega |h(t, \theta, \phi; q)|^2 = \sum_{\ell,m} |h^{\ell,m}(t; q)|^2, \quad (2)$$

to be maximum at $t = 0$. After enforcing this alignment scheme we interpolate the waveform mode amplitudes and phases onto an array of uniformly spaced times in $[-2750, 100]M$, with $\Delta t = 0.1M$. Finally, we align the initial gravitational wave mode phases by performing a simulation-dependent, constant (in time) physical rotation about the z -axis so that $\varphi^{2,2}(t_i) = \varphi^{2,-2}(t_i)$, which fixes a physical rotation up to multiples of π . We resolve the ambiguity by requiring $\varphi^{2,1}(t_i) \in (-\pi, 0]$. Waveform truncation errors, after performing this surrogate alignment scheme, are shown in Fig. 2. In what follows, we call “truncation error after surrogate alignment” simply “truncation error.”

Building the surrogate– Each $m > 0$ mode, $h^{\ell,m}(t; q)$, is modeled separately while (due to reflection symmetry about the orbital plane) $m < 0$ modes are evaluated using $h^{\ell,-m}(t; q) = (-1)^{\ell} h^{\ell,m}(t; q)^*$. We model all $m \neq 0$ modes but keep only those yielding smaller surrogate errors $\delta h^{\ell,m}$ compared to setting the mode to zero. Table II lists our modeled modes and their errors.

Our complete surrogate waveform model is defined by $h_S(t, \theta, \phi; q) = \sum_{\ell,m} h_S^{\ell,m}(t; q) {}_{-2}Y_{\ell m}(\theta, \phi)$ where

$$h_S^{\ell,m}(t; q) = A_S^{\ell,m}(t; q) e^{-i\varphi_S^{\ell,m}(t; q)}, \quad (3)$$

$$X_S^{\ell,m}(t; q) = \sum_{i=1}^{N_X} B_{X,i}^{\ell,m}(t) X_i^{\ell,m}(q), \quad X = \{A, \varphi\}.$$

Unlike Ref. [27], we construct a reduced basis representation for the waveform amplitudes and phases separately, instead of the waveforms themselves [37]. Here, the $\{B_{X,i}^{\ell,m}\}_{i=1}^{N_X}$ are computed off-line from the SpEC waveforms [27]. At a set of N_X specially selected times $\{T_{X,i}^{\ell,m}\}_{i=1}^{N_X}$, which are the empirical interpolant nodes [27, 51], the functions $X_i^{\ell,m}(q) \approx X^{\ell,m}(T_{X,i}^{\ell,m}; q)$ approximate the parametric variation of the amplitudes and

¹ We integrate Ψ_4 twice in the (dimensionless) frequency domain by dividing $-\Psi_4^{\ell,m}(f)$ by $[2\pi \max(f, 2f_0/3)]^2$, where f_0 is the initial GW mode frequency.

² Throughout, we exclude $m = 0$ modes because (non-oscillatory) Christodoulou memory is not accumulated sufficiently in current NR simulations [49].

phases (via fitting). A thorough discussion of surrogate model building steps is presented in [27]. When evaluating the surrogate at a particular mass ratio, the fits are evaluated first to determine the amplitudes and phases at their respective interpolating times $\{T_{X,i}^{\ell m}\}_{i=1}^{N_X}$. The remaining operations yield the surrogate model prediction, $h_S(t, \theta, \phi; q)$.

To find each $X_i^{\ell m}(q)$ we perform least-squares fits to the 22 data points, $\{X^{\ell m}(T_{X,i}^{\ell m}; q_j)\}_{j=1}^{22}$. All fits except odd m mode amplitudes use 5th degree polynomials in the symmetric mass ratio, $\nu = q/(1+q)^2$. For odd m modes, the amplitude approaches 0 and its derivative with respect to ν diverges as $q \rightarrow 1$ (or $\nu \rightarrow 1/4$). Consequently, we use $A_i^{\ell m}(\nu) = \sum_{n=1/2,1}^5 a_n^{\ell m} (1-4\nu)^n$ to account for this behavior. The waveform phases of odd m modes at $q = 1$, which are undefined, are excluded when fitting for each $\varphi_i^{\ell m}(q)$.

Assessing surrogate errors— We next assess the surrogate’s predictive quality. To quantify the error in the surrogate model itself, as opposed to its usage in a data analysis study, we do *not* minimize the errors over relative time and phase shifts here.

A first test is a consistency check to reproduce the 22 input SpEC waveforms used to build the surrogate. These errors are shown in Fig. 4 (red squares) and are comparable to or smaller than the *largest* SpEC truncation errors (black circles).

A more stringent test is the leave-one-out cross-validation (LOOCV) study [52]. For each simulated mass ratio q_i , we build a temporary *trial surrogate* using the other 21 waveforms, evaluate the trial surrogate at q_i , and compare the prediction with the SpEC waveform for q_i . Hence, the trial surrogate’s error at q_i should serve as an upper bound for the full surrogate trained on all 22 waveforms. Repeating this process for all possible 20 LOOCV tests³ results in Fig. 4 (blue triangles). Despite the i th trial surrogate having no information about the waveform at q_i , the errors remain comparable to the *largest* SpEC truncation errors. The LOOCV errors are typically twice as large as the full surrogate ones confirming the former as bounds for the latter. Relative errors for selected modes are shown in Table II. While weaker modes have larger relative errors, their power contribution is small enough that the error in the full surrogate waveform, δh , is nearly identical to the SpEC resolution error.

A third test is to compare the surrogate waveforms to those of a second surrogate, built from the second highest resolution SpEC waveforms. The resulting comparison is shown in Fig. 4 (cyan line). These errors are comparable to SpEC waveform truncation errors (black circles).

(ℓ, m)	Surrogate		NR		(ℓ, m)	Surrogate		NR	
	Max	Mean	Max	Mean		Max	Mean	Max	Mean
(2, 2)	0.36	0.07	0.36	0.08	(3, 2)	100	17	1.7	0.43
(2, 1)	29	3.4	4.1	0.54	(4, 4)	7.4	2.2	20	2.1
(3, 3)	53	4.1	11	0.94	All	0.42	0.12	0.40	0.10

TABLE II. Relative mode errors, reported as $10^3 \times \|h_S^{\ell, m}(q) - h^{\ell, m}(q)\|^2 / \|h^{\ell, m}(q)\|^2$, from the leave-one-out surrogates. Only those modes which contribute greater than 0.02% to the full waveform’s time-domain power are used in the computation of the max and mean, except for ‘All’ which is just δh . Our surrogate also includes the (3, 1), (4, [2, 3]), (5, [3, 4, 5]), (6, [4, 5, 6]), (7, [5, 6, 7]), and (8, [7, 8]) modes. Weaker modes typically have relative errors between 1% and 35%.

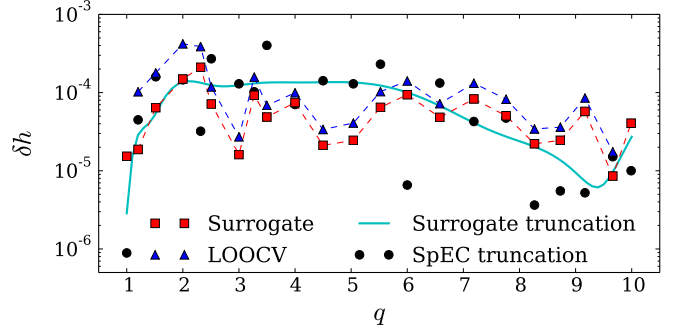


FIG. 4. Waveform differences between the two highest SpEC resolutions (black circles), surrogates built from the two highest SpEC resolutions (cyan line), the full surrogate and SpEC (red squares), and leave-one-out trial surrogates and SpEC (blue triangles). The largest surrogate error is for $q = 2$, for which the (2, 2) mode is shown in Fig. 1.

We find that the surrogate building process is robust to resolution differences. Furthermore, the surrogate can be improved using NR waveforms of higher accuracy.

We perform a final test and construct surrogates using the first N selected mass ratios (from Table I) as input waveforms, leaving $22 - N$ mass ratios with which to test. We find the total surrogate error decreases exponentially with N and is comparable to the SpEC truncation error after using 15 waveforms. Some modes (e.g., (2, 2)) are fully resolved after as few as 7 waveforms.

Comparison to EOB— For data analysis purposes, we compare our surrogate with EOBNRv2 [19] and SEOBNRv2 [21] models (generated from a current implementation⁴ in LAL [38]). In Fig. 5, we show the unfaithfulness

$$1 - \max_{\delta\varphi, \delta t} \text{Re} \int_{15\text{Hz}}^{\infty} df \frac{\hat{h}_1(f; \theta, \varphi) \hat{h}_2^*(f; \theta, \varphi + \delta\varphi) e^{2\pi i f \delta t}}{S_n(f)} \quad (4)$$

³ We omit the smallest and largest mass ratios here as the corresponding trial surrogates would extrapolate to their values.

⁴ We find that very small changes ($\sim 10^{-12}$) in the minimum frequency or the total mass can have unexpectedly large changes in the unfaithfulness ($\sim 10^{-4}$)

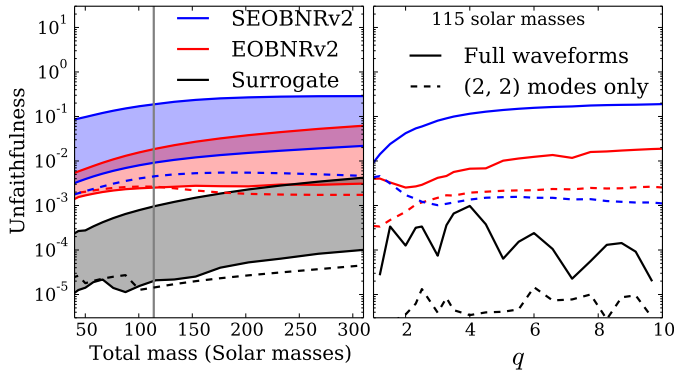


FIG. 5. Unfaithfulness, from Eq. (4), comparing SpEC with our surrogate, EOBNRv2, and SEOBNRv2 models using all available $m \neq 0$ modes. Dashed lines show the unfaithfulness for (2, 2) modes only. All waveforms are Planck-tapered [54] for $t \in [-2750, -2500]M$ and $t \in [50, 90]M$. For the full multi-modal waveforms, we maximize the unfaithfulness over θ and φ for the worst-case scenario. We use the “+” polarization, which is non-zero for all (θ, φ) . **Left:** The shaded regions contain all 22 mass ratios, while the dashed lines maximize over mass ratio. The vertical grey line is the minimum total mass ($\approx 115M_\odot$) ensuring all (2, 2) modes start with ≤ 15 Hz at the end of the first tapering window. **Right:** Unfaithfulness for a $115M_\odot$ binary.

of the surrogate and the two EOB models against the NR waveforms. Here, \hat{h} is the normalized Fourier transform of h (such that a waveform’s unfaithfulness with itself gives 0), and $S_n(f)$ the advanced LIGO zero-detuned high power sensitivity noise curve [53]. The surrogate is more faithful than both EOB models for all cases considered. Since SEOBNRv2 only provides (2, ± 2) modes, it performs worst for large total masses where additional modes become important. All models predict the (2, 2) mode with an unfaithfulness $< 1\%$ for $q \in [1, 10]$ at $115M_\odot$, however the EOB models are limited by the availability of subdominant modes.

Discussion— We have built a surrogate model for NR non-spinning BBH merger waveforms generated by SpEC. On a standard 2015 single core computer, all 77 modes with $2 \leq \ell \leq 8$ are evaluated in ≈ 0.5 sec (≈ 0.01 sec for a single mode) providing a factor of $\sim 10^6$ – 10^8 speedup compared to SpEC. Importantly, this is achieved with only a *small* loss in accuracy. Like other data-driven modeling strategies, our surrogate is valid only within the training intervals, namely, $q \in [1, 10]$ and $t/M \in [-2570, 100]$. Therefore, within the training intervals, our surrogate model generates BBH merger waveforms that are equivalent to SpEC outputs up to numerical error and a small modeling error.

NR surrogates can be used for multiple-query applications in gravitational wave data analysis such as detector-specific template-bank (re-)generation and parameter estimation. Our surrogate, and more generally the results of this paper, open up the exciting possibility of perform-

ing, for example, parameter estimation with multi-modal NR waveforms (with hybridization, if needed). Parameter estimation studies seeking to incorporate model error may benefit from the surrogate’s relatively straightforward characterization and assessment of uncertainty from a combination of the surrogate’s and SpEC’s systematic and numerical errors. We anticipate NR surrogate modeling to complement traditional strategies [15–24, 26] by providing unlimited high-fidelity approximations of NR waveforms with which to calibrate, refine and make comparisons. Building NR surrogates of precessing BBH merger waveforms, which may be modeled from the parameters specially selected in [55], offer a promising avenue for modeling the full 7 dimensional BBH parameter space. The surrogate model described in this paper is available for download at [56, 57].

We thank Mike Boyle, Alessandra Buonanno, Collin Capano, Jan Hesthaven, Jason Kaye, Geoffrey Lovelace, Lee Lindblom, Tom Lored, Christian Ott, Yi Pan, Harald Pfeiffer, Rory Smith, and Nicholas Taylor for many useful discussions throughout this project. This work was supported in part by NSF grants CAREER PHY-0956189, PHY-1068881, PHY-1005655, PHY-1440083, PHY-1404569, and AST-1333520 to Caltech, NSF grants PHY-1306125 and AST-1333129 to Cornell University, NSF grant PHY-1500818 to the University of California at San Diego, NSF grants PHY-1208861 and PHY-1316424 to the University of Maryland (UMD), NSERC of Canada, and the Sherman Fairchild Foundation. Computations were performed on the Zwicky cluster at Caltech, which is supported by the Sherman Fairchild Foundation and by NSF award PHY-0960291. Portions of this research were carried out at the Center for Scientific Computation and Mathematical Modeling cluster at UMD.

-
- [1] F. Pretorius, *Phys. Rev. Lett.* **95**, 121101 (2005), [arXiv:gr-qc/0507014 \[gr-qc\]](#).
 - [2] M. Campanelli, C. Lousto, P. Marronetti, and Y. Zlochower, *Phys. Rev. Lett.* **96**, 111101 (2006), [arXiv:gr-qc/0511048 \[gr-qc\]](#).
 - [3] J. G. Baker, J. Centrella, D.-I. Choi, M. Koppitz, and J. van Meter, *Phys. Rev. Lett.* **96**, 111102 (2006), [arXiv:gr-qc/0511103 \[gr-qc\]](#).
 - [4] B. Aylott, J. G. Baker, W. D. Boggs, M. Boyle, P. R. Brady, *et al.*, *Class. Quant. Grav.* **26**, 165008 (2009), [arXiv:0901.4399 \[gr-qc\]](#).
 - [5] P. Ajith, M. Boyle, D. A. Brown, B. Bruggmann, L. T. Buchman, *et al.*, *Class. Quantum Grav.* **29**, 124001 (2012).
 - [6] A. H. Mroue, M. A. Scheel, B. Szilagyi, H. P. Pfeiffer, M. Boyle, D. A. Hemberger, L. E. Kidder, G. Lovelace, S. Ossokine, N. W. Taylor, A. Zenginoglu, L. T. Buchman, T. Chu, E. Foley, M. Giesler, R. Owen, and S. A. Teukolsky, *Phys. Rev. Lett.* **111**, 241104 (2013),

- arXiv:1304.6077 [gr-qc].
- [7] I. Hinder *et al.* (The NRAR Collaboration), *Classical and Quantum Gravity* **31**, 025012 (2014), arXiv:1307.5307 [gr-qc].
 - [8] L. Pekowsky, R. O’Shaughnessy, J. Healy, and D. Shoemaker, *Phys. Rev. D* **88**, 024040 (2013), arXiv:1304.3176 [gr-qc].
 - [9] J. Aasi *et al.* (The LIGO Scientific Collaboration, the Virgo Collaboration, the NINJA-2 Collaboration), *Class. Quantum Grav.* **31**, 115004 (2014), arXiv:1401.0939 [gr-qc].
 - [10] <http://www.black-holes.org/waveforms> ().
 - [11] G. M. Harry (for the LIGO Scientific Collaboration), *Class. Quantum Grav.* **27**, 084006 (2010).
 - [12] The Virgo Collaboration, “Advanced Virgo Baseline Design,” (2009), [VIR-0027A-09].
 - [13] J. Abadie, B. P. Abbott, R. Abbott, M. Abernathy, T. Accadia, F. Acernese, C. Adams, R. Adhikari, P. Ajith, B. Allen, and et al., *Classical and Quantum Gravity* **27**, 173001 (2010), arXiv:1003.2480 [astro-ph.HE].
 - [14] P. Kumar, I. MacDonald, D. Brown, H. Pfeiffer, K. Cannon, M. Boyle, L. Kidder, A. Mroue, M. Scheel, B. Szilágyi, and A. Zenginoglu, *Phys. Rev. D* **89**, 042002 (2014), 1310.7949.
 - [15] A. Buonanno and T. Damour, *Phys. Rev. D* **59**, 084006 (1999), arXiv:gr-qc/9811091 [gr-qc].
 - [16] T. Damour and A. Nagar, *Phys. Rev. D* **79**, 081503 (2009), arXiv:0902.0136 [gr-qc].
 - [17] A. Buonanno, Y. Pan, H. P. Pfeiffer, M. A. Scheel, L. T. Buchman, and L. E. Kidder, *Phys. Rev. D* **79**, 124028 (2009), arXiv:0902.0790 [gr-qc].
 - [18] Y. Pan, A. Buonanno, L. T. Buchman, T. Chu, L. E. Kidder, H. P. Pfeiffer, and M. A. Scheel, *Phys. Rev. D* **81**, 084041 (2010), arXiv:0912.3466 [gr-qc].
 - [19] Y. Pan, A. Buonanno, M. Boyle, L. T. Buchman, L. E. Kidder, *et al.*, *Phys. Rev. D* **84**, 124052 (2011), arXiv:1106.1021 [gr-qc].
 - [20] T. Damour, A. Nagar, and S. Bernuzzi, *Phys. Rev. D* **87**, 084035 (2013), arXiv:1212.4357 [gr-qc].
 - [21] A. Taracchini, Y. Pan, A. Buonanno, E. Barausse, M. Boyle, T. Chu, G. Lovelace, H. P. Pfeiffer, and M. A. Scheel, *Phys. Rev. D* **86**, 024011 (2012), arXiv:1202.0790 [gr-qc].
 - [22] P. Ajith, S. Babak, Y. Chen, M. Hewitson, B. Krishnan, J. T. Whelan, B. Brügmann, P. Diener, J. Gonzalez, M. H. S. Husa, M. Koppitz, D. Pollney, L. Rezzolla, L. Santamaría, A. M. Sintes, U. Sperhake, and J. Thornburg, *Class. Quantum Grav.* **24**, S689 (2007), arXiv:0704.3764 [gr-qc].
 - [23] L. Santamaría, F. Ohme, P. Ajith, B. Brügmann, N. Dornband, M. Hannam, S. Husa, P. Mösta, D. Pollney, C. Reisswig, E. L. Robinson, J. Seiler, and B. Krishnan, *Phys. Rev. D* **82**, 064016 (2010), arXiv:1005.3306 [gr-qc].
 - [24] R. Sturani, S. Fischetti, L. Cadonati, G. Guidi, J. Healy, *et al.*, *J. Phys. Conf. Ser.* **243**, 012007 (2010), arXiv:1005.0551 [gr-qc].
 - [25] M. Hannam, P. Schmidt, A. Boh, L. Haegel, S. Husa, *et al.*, *Phys. Rev. Lett.* **113**, 151101 (2014), arXiv:1308.3271 [gr-qc].
 - [26] J. Abadie *et al.* (The LIGO Scientific Collaboration and the Virgo Collaboration), *Phys. Rev. D* **83**, 122005 (2011), arXiv:1102.3781 [gr-qc].
 - [27] S. E. Field, C. R. Galley, J. S. Hesthaven, J. Kaye, and M. Tiglio, *Phys. Rev. X* **4**, 031006 (2014), arXiv:1308.3565 [gr-qc].
 - [28] J. Kaye, *The interpolation of gravitational waveforms*, Ph.D. thesis, Brown University (2012).
 - [29] Y. Maday, A. T. Patera, and G. Turinici, *J. Sci. Comput.* **17**, 437 (2002).
 - [30] K. Veroy, C. Prud’homme, and A. T. Patera, *Comptes Rendus Mathématique* **337**, 619 (2003).
 - [31] C. Prud’homme, D. V. Rovas, K. Veroy, L. Machiels, Y. Maday, A. T. Patera, and G. Turinici, *Journal of Fluids Engineering* **124**, 70 (2002).
 - [32] Y. Chen, J. S. Hesthaven, Y. Maday, and J. Rodríguez, *SIAM J. Sci. Comput.* **32**, 970 (2010).
 - [33] A. Quarteroni, G. Rozza, and A. Manzoni, *Journal of Mathematics in Industry* **1**, 1 (2011).
 - [34] <http://www.black-holes.org/SpEC.html>.
 - [35] M. A. Scheel, M. Giesler, D. A. Hemberger, G. Lovelace, K. Kuper, M. Boyle, B. Szilágyi, and L. E. Kidder, *Classical and Quantum Gravity* **32**, 105009 (2015), arXiv:1412.1803 [gr-qc].
 - [36] B. Szilágyi, *Int. J. Mod. Phys. D* **23**, 1430014 (2014), arXiv:1405.3693 [gr-qc].
 - [37] M. Pürrer, *Class. Quantum Grav.* **31**, 195010 (2014), arXiv:1402.4146 [gr-qc].
 - [38] L. S. Collaboration, “LSC Algorithm Library software packages LAL, LALWRAPPER, and LALAPPS,” .
 - [39] P. Binev, A. Cohen, W. Dahmen, R. A. DeVore, G. Petrova, and P. Wojtaszczyk, *SIAM J. Math. Analysis* **43**, 1457 (2011).
 - [40] S. E. Field, C. R. Galley, F. Herrmann, J. S. Hesthaven, E. Ochsner, *et al.*, *Phys. Rev. Lett.* **106**, 221102 (2011), arXiv:1101.3765 [gr-qc].
 - [41] H. P. Pfeiffer, D. A. Brown, L. E. Kidder, L. Lindblom, G. Lovelace, and M. A. Scheel, *Class. Quantum Grav.* **24**, S59 (2007), gr-qc/0702106.
 - [42] A. Buonanno, L. E. Kidder, A. H. Mroué, H. P. Pfeiffer, and A. Taracchini, *Phys. Rev. D* **83**, 104034 (2011), arXiv:1012.1549 [gr-qc].
 - [43] A. H. Mroué and H. P. Pfeiffer, (2012), arXiv:1210.2958 [gr-qc].
 - [44] N. T. Bishop, R. Gomez, L. Lehner, M. Maharaj, and J. Winicour, *Phys. Rev. D* **56**, 6298 (1997), arXiv:gr-qc/9708065.
 - [45] M. C. Babiuc, B. Szilágyi, J. Winicour, and Y. Zlochower, *Phys. Rev. D* **84**, 044057 (2011), arXiv:1011.4223 [gr-qc].
 - [46] J. Winicour, *Living Rev. Rel.* **12** (2009).
 - [47] C. Reisswig and D. Pollney, *Class. Quant. Grav.* **28**, 195015 (2011), arXiv:1006.1632 [gr-qc].
 - [48] N. W. Taylor, M. Boyle, C. Reisswig, M. A. Scheel, T. Chu, L. E. Kidder, and B. Szilágyi, *Phys. Rev. D* **88**, 124010 (2013), arXiv:1309.3605 [gr-qc].
 - [49] M. Favata, *Phys. Rev. D* **80**, 024002 (2009), arXiv:0812.0069 [gr-qc].
 - [50] A. H. Mroué, H. P. Pfeiffer, L. E. Kidder, and S. A. Teukolsky, *Phys. Rev. D* **82**, 124016 (2010), arXiv:1004.4697 [gr-qc].
 - [51] Y. Maday, N. C. Nguyen, A. T. Patera, and S. H. Pau, *Communications on Pure and Applied Analysis* **8**, 383 (2009).
 - [52] T. Hastie, R. Tibshirani, and J. Friedman, *The Elements of Statistical Learning*, Springer Series in Statistics (Springer New York Inc., New York, NY, USA, 2001).

- [53] D. Shoemaker (LIGO Collaboration), “**Advanced LIGO anticipated sensitivity curves**,” (2010), LIGO Document T0900288-v3.
- [54] D. McKechnan, C. Robinson, and B. Sathyaprakash, **Class. Quant. Grav.** **27**, 084020 (2010), arXiv:1003.2939 [gr-qc].
- [55] J. Blackman, B. Szilagyi, C. R. Galley, and M. Tiglio, **Phys.Rev.Lett.** **113**, 021101 (2014), arXiv:1401.7038 [gr-qc].
- [56] “Simulating eXtreme Spacetimes,” (), <http://www.black-holes.org/surrogates/>.
- [57] “Gwsurrogate,” <https://pypi.python.org/pypi/gwsurrogate/>.